

---

**NOTE**

# Simple Auto-Calibrated Gradient Delay Estimation From Few Spokes Using Radial Intersections (RING)

Sebastian Rosenzweig<sup>1\*</sup> | H. Christian M. Holme<sup>1,2</sup> |  
Martin Uecker<sup>1,2</sup>

<sup>1</sup>Institute for Diagnostic and Interventional Radiology, University Medical Center Göttingen, Göttingen, Germany

<sup>2</sup>German Centre for Cardiovascular Research (DZHK), Partner site Göttingen, Göttingen, Germany

## Correspondence

Sebastian Rosenzweig, University Medical Center Göttingen, Institute for Diagnostic and Interventional Radiology, Robert-Koch-Str. 40, 37075 Göttingen, Germany  
Email: sebastian.rosenzweig@med.uni-goettingen.de

Submitted to Magnetic Resonance in Medicine as a Note. **Word count: Abstract 170, Body 2921.**

## Funding information

**Purpose:** To develop a simple and robust tool for the estimation of gradient delays from highly undersampled radial k-space data.

**Theory:** In radial imaging gradient delays induce parallel and orthogonal trajectory shifts, which can be described using an ellipse model. The intersection points of the radial spokes, which can be estimated by spoke-by-spoke comparison of k-space samples, distinctly determine the parameters of the ellipse. Using the proposed method (RING), these parameters can be obtained using a least-squares fit and utilized for the correction of gradient delays.

**Methods:** The functionality and accuracy of the proposed RING method is validated and compared to correlation-based gradient-delay estimation from opposing spokes using numerical simulations, phantom and in vivo heart measurements.

**Results:** In all experiments, RING robustly provides accurate gradient delay estimations even for as few as three radial spokes.

**Conclusion:** The simple and straightforward to implement RING method provides accurate gradient delay estimation for highly undersampled radial imaging.

## KEYWORDS

trajectory correction, radial imaging, gradient delay, artifacts, system imperfections, RING

## 1 | INTRODUCTION

In today's clinical practice almost all magnetic resonance imaging (MRI) techniques are based on Cartesian trajectories. Nevertheless, in the recent years non-Cartesian trajectories, in particular radial acquisitions, drew increasing interest among the scientific community for their motion robustness and milder undersampling artifacts and proofed potential for a significant imaging speed-up [1, 2, 3, 4, 5]. Although the benefits of radial trajectories seem evident, for various reasons they did not yet find widespread application in clinical routine. One reason is the higher sensitivity to system imperfections such as eddy-current-induced gradient delays, that lead to deviations from the nominal sampling locations [6]. To tackle this problem, a variety of different trajectory error compensation strategies have been developed. One approach is to measure the actual k-space trajectory during each measurement using specialized hardware, which is highly effective but expensive and not always practical [7, 8]. Alternatively, calibration scans can be utilized to fully characterize the gradient system impulse response function (GIRF) of the scanner [9, 10, 11, 12]. However, as these methods have not yet been adopted by the vendors they require significant implementation efforts and are difficult to integrate into a complete workflow. Furthermore, GIRF-based methods cannot capture sequence or protocol dependent temporal variations of the gradient system e.g. through heating, and the characterization must be repeated regularly to compensate long-term system variances.

Other approaches have been designed particularly for error compensation in radial imaging. Iterative, parallel imaging-based methods developed by Deshmane et al. [13] and Wech et al. [14] exploit correlations in the receive channels using GRAPPA operator gridding [15] and shift the samples or the trajectory position until a certain condition is fulfilled. Both methods are data driven and therefore can be used to retrospectively detect and compensate transient trajectory errors. These methods require good estimates for the gridding operators, which in turn demands sufficient in-plane coil sensitivity variation and a certain number of spokes for auto-calibration. These conditions might not always be given, as e.g. in interactive real-time MRI the imaging plane is repeatedly being rotated and shifted [16, 17, 18, 19]. Recently, Jiang et al. [20] introduced a framework which simultaneously estimates gradient delays and coil sensitivities using an alternating minimization approach. This method inspired by SAKE [21] uses a computationally rather demanding low-rank constraint in conjunction with the Gauss-Newton method to solve a non-linear optimization problem. Furthermore, two more general algorithms have been proposed that combine trajectory correction and image reconstruction [22, 23]. However, in the approach of Mani et al. [22] prior knowledge about the coil sensitivities is necessary. Moreover, both algorithms might be difficult to combine with other image reconstruction methods.

A noticeable alternative to the above mentioned rather elaborate trajectory correction techniques is the Adaptive method developed by Block and Uecker [24] for radial imaging. Because of its intuitive approach, its robustness and accuracy and the straight forward implementation it found widespread acceptance and application [25, 26, 27, 28, 5]. The method requires calibration scans where pairs of opposed spokes with varying orientation are acquired. Then, the sample shift along the readout direction is calculated by performing a cross-correlation of the opposed spokes. The shifts are fitted to a linear ellipse model [6, 27] and compensated for in the gridding procedure. Recently, it was shown that the same approach can be used to estimate the gradient delays from the data itself without the need for calibration scans. This auto-calibrated variant, here dubbed AC-Adaptive method, was described by Untenberger et al. [28], applied in several publications, e.g. [29, 30, 31], and studied in [32]. Instead of using perfectly anti-parallel spokes, the AC-Adaptive method takes spokes from the actual radial acquisition which are only approximately anti-parallel to estimate the shifts. This allows for real-time and retrospective gradient delay correction which can be applied to e.g. interactive real-time MRI or to compensate gradient delay changes due to coil heating. However, the present work shows that the AC-Adaptive method is not fully consistent with the ellipse model which it is based on. In settings with oblique slices and/or non-isotropic delays of the physical gradients, the spokes will experience both a shift in read-out

direction and orthogonal to it. Due to the latter, even perfectly opposed spokes will not cover the same k-space line which leads to inconsistencies in the cross-correlation calculation. Furthermore, the AC-Adaptive method cannot provide stable gradient delay estimates given only very few spokes, as then no nearly opposed spoke pairs exist.

The aim of this work is to develop a simple yet accurate and robust gradient delay estimation tool which also works for very few spokes. We show that our method, which uses Radial spoke INtersections for Gradient delay estimation (RING), outperforms the AC-Adaptive method in all investigated numerical simulations, phantom and in vivo heart measurements and provides precise gradient delay estimates even for as few as 3 spokes.

## 2 | THEORY

### The gradient delay ellipse model.

Peters et al. showed that in radial imaging, linear eddy current effects delay the start of the readout gradients which induces both a parallel and an orthogonal shift to the nominal k-space trajectory, while the projection direction is not affected [6]. Moussavi et al. [27] proposed a simple model to describe this spoke shift as a vector

$$\delta \mathbf{k} := \mathbf{S} \hat{\mathbf{n}}_{\theta}, \quad (1)$$

$$\hat{\mathbf{n}}_{\theta} := \begin{pmatrix} \cos \theta \\ \sin \theta \end{pmatrix}, \quad (2)$$

$$\mathbf{S} := \begin{pmatrix} S_x & S_{xy} \\ S_{xy} & S_y \end{pmatrix} \quad (3)$$

with  $\theta$  the projection angle and  $\hat{\mathbf{n}}$  the normalized projection direction.  $S_x$  and  $S_y$  capture the delays in the axial case whereas  $S_{xy}$  guarantees three-dimensional rotational invariance and particularly accounts for the interaction of all three physical gradients when measuring oblique slices. For a detailed derivation please consider the appendix. The goal of this work is to efficiently determine the parameters  $S_x$ ,  $S_y$  and  $S_{xy}$ , which can then be used to calculate the actual (shifted) trajectory needed for accurate gridding in image reconstruction.

Let  $N_{\text{samp}}$  be the number of samples in readout direction and  $N_{\text{sp}}$  the number of spokes used for gradient delay estimation. Then, the sample positions in units of  $1/\text{FOV}$  of a spoke with projection angle  $\theta_i, i \in \{1, \dots, N_{\text{sp}}\}$ , can be modeled using the parametric linear equation

$$\mathbf{r}_{\theta_i} = \mathbf{S} \hat{\mathbf{n}}_{\theta_i} + a_{\theta_i} \hat{\mathbf{n}}_{\theta_i} \quad (4)$$

with  $a_{\theta_i} = [-N_{\text{samp}}/2, N_{\text{samp}}/2 - 1]$ . The ellipse defined by Eq. (1) determines the position  $\mathbf{r}_{\theta_i}(a_{\theta_i} = 0)$  of the shifted spokes.

Fig. 1 depicts a schematic of actual k-space trajectories for different delays  $\mathbf{S}$ . If no gradient delays are present (top-left) the spokes are not shifted at all. For isotropic delays in the axial case (top-right) the spokes are translated in readout direction only. For anisotropic delays (bottom-left) and/or oblique slices (bottom-right) the spokes experience both a readout-shift and an orthogonal shift and no longer intersect in the k-space center. The intersection points of the spokes relative to their DC component uniquely define the shift matrix  $\mathbf{S}$ .

### Determination of $S_x$ , $S_y$ and $S_{xy}$ .

The intersection point of the spokes  $r_{\theta_i}$  and  $r_{\theta_j}$  yield a conditional equation for  $S$ :

$$r_{\theta_i}(a'_{\theta_i}) \stackrel{!}{=} r_{\theta_j}(a'_{\theta_j}), \quad (5)$$

$$S(\hat{\mathbf{n}}_{\theta_i} - \hat{\mathbf{n}}_{\theta_j}) = a'_{\theta_j} \hat{\mathbf{n}}_{\theta_j} - a'_{\theta_i} \hat{\mathbf{n}}_{\theta_i}. \quad (6)$$

To facilitate calculations, we introduce the definitions

$$\mathbf{s} := \begin{pmatrix} S_x \\ S_y \\ S_{xy} \end{pmatrix}, \quad (7)$$

$$\hat{\mathbf{n}}_{\theta_i} - \hat{\mathbf{n}}_{\theta_j} := \begin{pmatrix} \xi_1 \\ \xi_2 \end{pmatrix}, \quad \mathbf{A} := \begin{pmatrix} \xi_1 & 0 & \xi_2 \\ 0 & \xi_2 & \xi_1 \end{pmatrix}, \quad (8)$$

$$\mathbf{b} := a'_{\theta_j} \hat{\mathbf{n}}_{\theta_j} - a'_{\theta_i} \hat{\mathbf{n}}_{\theta_i}, \quad (9)$$

and rearrange Eq. (6)

$$\mathbf{A} \mathbf{s} = \mathbf{b}. \quad (10)$$

If  $N_{\text{sp}} > 2$ , Matrix  $\mathbf{A}$  and vector  $\mathbf{b}$  can be extended to contain all considered intersection points. Then, the system of equations Eq. (10) for  $\mathbf{s}$  is overdetermined and  $\mathbf{s}$  can be obtained by a least-squares fit using the pseudo-inverse

$$\mathbf{s} = (\mathbf{A}^T \mathbf{A})^{-1} \mathbf{A}^T \mathbf{b}, \quad (11)$$

where  $^T$  indicates the transpose.

### Determination of intersection points.

To obtain  $\mathbf{s}$  (Eq. (11)) the values for  $a'_\theta$  in Eq. (6) must be determined from the measured data. Since the k-space value at the intersection point of two spokes should be identical except for noise in all channels, the values for  $a'_\theta$  can be obtained by comparing the actual complex sample values of the spokes. The sample pair for which the root-sum-of-squares difference over all channels is minimal is assumed to represent the intersection point. To guarantee accurate estimates for  $a'_\theta$  and thus  $\mathbf{s}$ , each spoke is retrospectively sub-sampled via Fourier interpolation and denoised: An inverse Fourier transform is used to obtain a spoke's image domain representation. As the readout direction is generally oversampled by a factor of 2, all samples outside of the central  $N_{\text{samp}} \times 0.6$  region can be set to zero to sinc-denoise k-space. Then, the data is zero-padded by  $N_{\text{pad}} \times N_{\text{samp}}$  (we propose  $N_{\text{pad}} = 100$ ) and the sub-sampled k-space is retrieved using another Fourier transform. As most of the energy is localized in the low spatial frequency region it is sensible to investigate only intersection points in the central region of k-space, which avoids inaccuracies due to noise. Therefore, only the intersection point of a spoke with its most orthogonal counterpart is considered, i.e. we search for the spoke pairs that best approximate an intersection angle of  $90^\circ$ . Then, the sample-wise comparison can be restricted to the central

$\beta \times N_{\text{pad}}$  (we propose  $\beta = 1.5$ ) samples of the spokes.

An analysis of the accuracy of the proposed method to determine the intersection points for different noise values and simulated phantoms is provided as supplementary material.

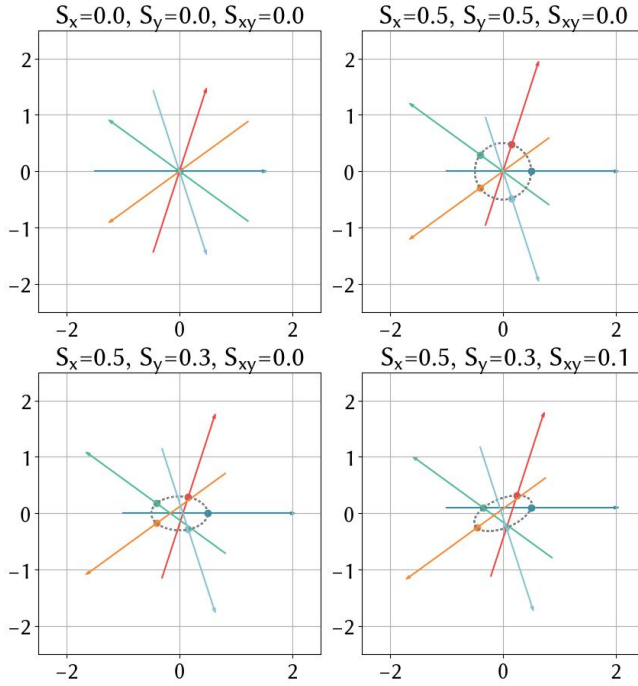


**FIGURE 1** Schematic of shifted k-space trajectories in units of  $1/\text{FOV}$  for different delays  $S_x$ ,  $S_y$  and  $S_{xy}$ . Exemplarily, 5 abridged spokes are depicted. The arrows point in readout direction and the DC sample of each spoke is highlighted by a dot. The ellipse determined by  $\delta k$  (Eq. (1)) is plotted as a dashed gray circle.

### 3 | METHODS

All measurements were performed on a SIEMENS Skyra 3T scanner, all reconstructions and the gradient delay estimation methods were implemented and performed using BART [33]. In our study we chose the RING parameters to be  $N_{\text{pad}} = 100$  and  $\beta = 1.5$ , which provided accurate and robust results throughout all experiments. In the interest of reproducible research, code and data to reproduce the experiments are made available on Github.<sup>1</sup>

#### Numerical Simulations.

To demonstrate the general functionality and accuracy of our method we performed a numerical Shepp-Logan k-space phantom study (oversampled readout samples 128, 8 channels) using a golden angle scheme and spokes shifted according to Eq. (1) with the nominal values  $s^{\text{iso}} = (0.3, 0.3, 0)$ ,  $s^{\text{ax}} = (0.3, -0.1, 0)$  and  $s^{\text{obl}} = (0.3, -0.1, 0.2)$  respectively.

<sup>1</sup><https://github.com/mrirecon/RING>

To quantify the estimation error  $\mathcal{E}(s, s_{N_{sp}}^{\text{est}})$  we used the L2 norm

$$\mathcal{E}(s, s_{N_{sp}}^{\text{est}}) := \sqrt{(S_x - S_x^{\text{est}})^2 + (S_y - S_y^{\text{est}})^2 + (S_{xy} - S_{xy}^{\text{est}})^2}, \quad (12)$$

where  $S$  stands for the nominal and  $S^{\text{est}}$  for the estimated shifts. We estimated the shifts using RING for all numbers of spokes in the range  $N_{sp} \in [3, 127]$  and performed the simulations for projection angles distributed over a half circle ( $\theta_i \in [0, \pi]$ ) and a full circle ( $\theta_i \in [0, 2\pi]$ ) [34].

For comparison we did the same experiments using the AC-Adaptive method.

### Phantom measurements.

For the measurement on a custom-made brick phantom we used the SIEMENS Head-Neck-20 coil and a FLASH sequence (FOV =  $256 \times 256 \text{ mm}^2$ , oversampled readout samples = 320, number of spokes = 159, TE/TR = 1.46/2.3 ms, slice thickness = 5 mm) with golden angle (half and full circle) acquisition. For the sake of better visibility of gradient delay artifacts, only 39 spokes were used for image reconstruction. The delays were estimated for all numbers of spokes in the range  $N_{sp} \in [3, 159]$  using both RING and the AC-Adaptive method for full circle acquisitions. For half circle acquisitions only RING is utilized. We used radial NLINV [35, 3] in combination with the corrected trajectories for image reconstruction. For each number of spokes  $N_{sp}$  the estimated delays  $s_{N_{sp}}^{\text{est}}$  were compared to  $s_{159}^{\text{est}}$  and the L2 errors  $\mathcal{E}(s_{159}^{\text{est}}, s_{N_{sp}}^{\text{est}})$  according to Eq. (12) were calculated.

### In vivo measurements.

We performed an in vivo measurement on a human heart (short-axis view, 30 channel thorax and spine coil, FLASH sequence, FOV =  $256 \times 256 \text{ mm}^2$ , oversampled readout samples = 320, TE/TR = 1.47/2.3 ms, slice thickness = 8 mm) using a full circle golden angle acquisition scheme. 75 consecutive spokes during the end-diastole were combined for image reconstruction with ENLIVE [36]. The gradient delays were estimated using RING and the AC-Adaptive method utilizing all numbers of spokes in the range  $N_{sp} \in [3, 75]$ . The L2 errors were calculated as described previously.

Human imaging was approved by the local ethics committee. Written informed consent was obtained from the subject before the imaging.

## 4 | RESULTS

### Numerical simulations.

The results of the numerical simulations are depicted in Fig. 2. The error  $\mathcal{E}(s, s_{N_{sp}}^{\text{est}})$  of the estimated gradient delays for different trajectory shifts using the AC-Adaptive method and RING are plotted over the number of spokes used for gradient delay estimation.

The RING method provides nearly perfect estimates for all investigated delays in half circle and full circle acquisitions, even if only three spokes are employed.

In contrast, the AC-Adaptive method delivers inaccurate gradient delay estimates for half circle acquisitions even if up to  $N_{sp} = 127$  spokes are used. For full circle acquisitions at least  $N_{sp} \approx 20$  spokes are necessary, to provide reasonable results. For fewer numbers of spokes the gradient delay error shows unpredictable behavior, which makes the estimates unreliable. By increasing the number of utilized spokes, the estimated delays converge to constant values. However, only the isotropic delay is estimated perfectly, whereas in the axial and oblique case a deviation from the optimal values remains.

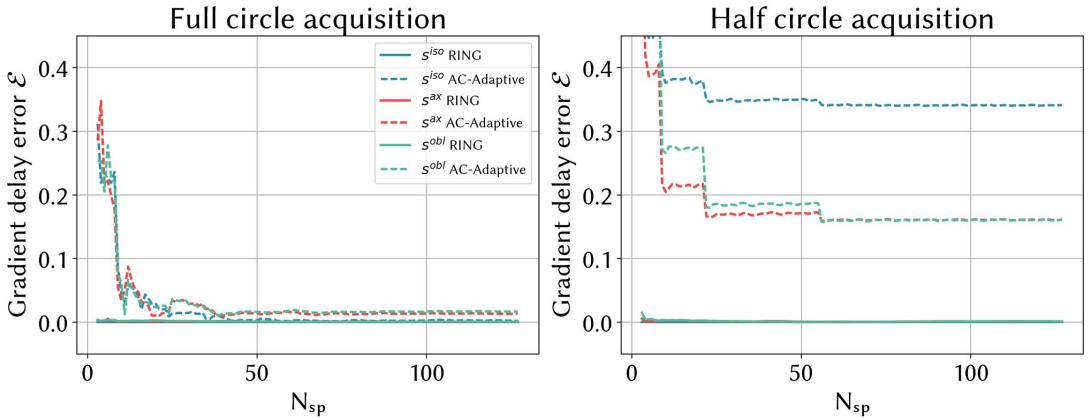


**FIGURE 2** Gradient delay error  $\mathcal{E}(s, s_{N_{sp}}^{est})$  (Eq. (12)) against the number of spokes utilized for gradient delay estimation using the RING and the AC-Adaptive method. Numerical k-space Shepp-Logan-phantom study with different nominal k-space trajectory shifts  $s^{iso} = (0.3, 0.3, 0)$ ,  $s^{ax} = (0.3, -0.1, 0)$  and  $s^{obl} = (0.3, -0.1, 0.2)$ . a) Full circle golden angle acquisition (projection angle  $\theta_j \in [0, 2\pi]$ ). b) Half circle golden angle acquisition (projection angle  $\theta_j \in [0, \pi]$ ).

### Phantom measurements.

The results of the phantom measurement and the corresponding gradient delay errors  $\mathcal{E}(s_{159}^{est}, s_{N_{sp}}^{est})$  over the number of spokes used for gradient delay estimation are provided in Fig. 3.

RING provides a good gradient delay estimation and thus, effective streaking artifact reduction even for only  $N_{sp} = 3$  spokes. The estimate is further improved when more spokes are utilized. However, the effect on the resulting image quality is only marginal, since the image is basically streaking free for  $N_{sp} = 3$  spokes already. Again, the method proves to be applicable to both full circle and half circle acquisition, although visual observation reveals slightly better results for full circle acquisitions with very few utilized spokes.

The AC-Adaptive method can only be applied in the full circle case, but does not provide accurate gradient delay estimates for few numbers of spokes where the results appear worse than the uncorrected image (not shown). Although the actual convergence value is not reached until  $N_{sp} = 37$  spokes, the results for  $N_{sp} = 15$  already look suitable, even if some streaking artifacts can still be observed at the top.

The actual gradient delay is not known but the convergence values for full circle acquisitions,  $s_{159}^{AC-Adaptive} = (0.336, 0.360, -0.021)$  and  $s_{159}^{RING} = (0.345, 0.384, -0.009)$ , are very similar for both methods. NUFFT reconstructions show an equivalent behavior and are depicted in Supplementary Figure 2.

### In vivo measurements.

Figure 4 shows the effects of the gradient delay correction on an in vivo measurement of the human heart, as well as the gradient delay error  $\mathcal{E}(s_{75}^{est}, s_{N_{sp}}^{est})$  for both the AC-Adaptive method and RING.

Using RING, even  $N_{sp} = 3$  are sufficient for effective streaking artifact elimination and the gradient delay error compared to the convergence value is small for all investigated numbers of spokes.

The AC-Adaptive method also provides robust streaking suppression for  $N_{sp} > 40$ . It estimates gradient delays close to convergence value for some smaller numbers of spokes, however, these results are not reliable as the gradient delay error shows large oscillations. For very few numbers of spokes, e.g.  $N_{sp} = 3$ , the estimates are useless and even amplify streaking artifacts.

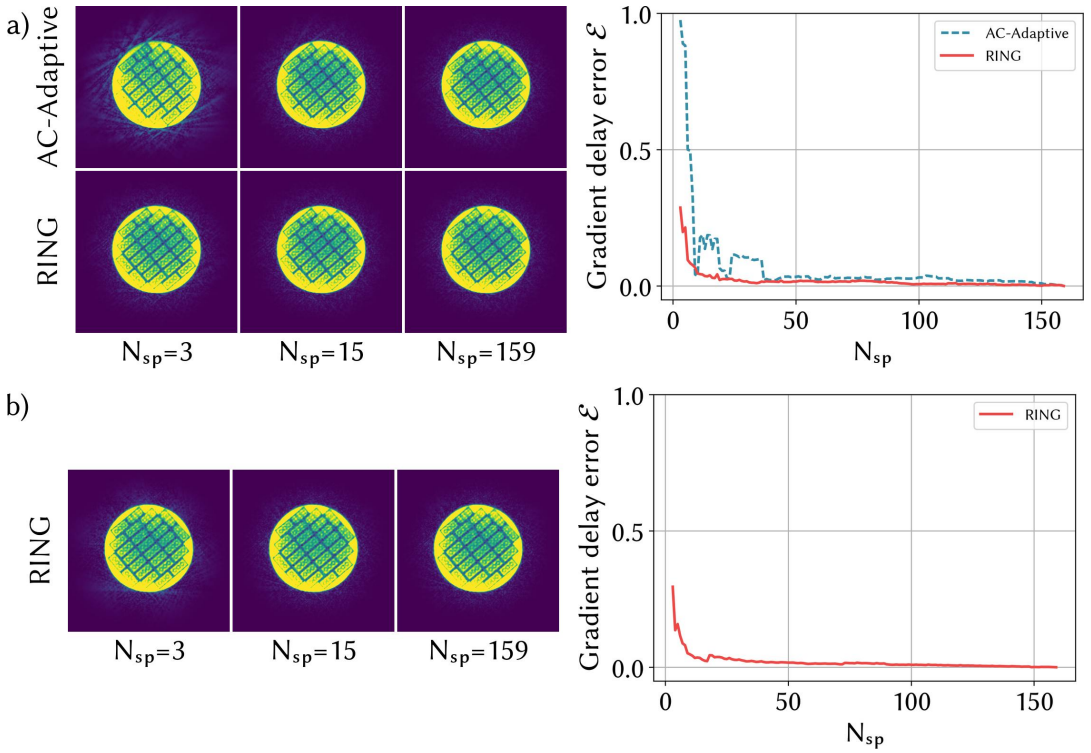


**FIGURE 3** NLINV reconstructions using 39 spokes of a brick phantom FLASH measurement with gradient delay correction estimated from  $N_{sp}$  number of spokes utilizing the AC-Adaptive method and the RING method. Besides, the gradient delay error  $\mathcal{E}(s_{159}^{est}, s_{N_{sp}}^{est})$  (Eq. (12)) against the number of spokes used for gradient delay estimation is depicted. a) Full circle golden angle acquisition (projection angle  $\theta_i \in [0, 2\pi]$ ). b) Half circle golden angle acquisition (projection angle  $\theta_i \in [0, \pi]$ ).

The convergence values of the gradient delay estimates are  $s_{75}^{RING} = (0.178, 0.068, 0.068)$  and  $s_{75}^{AC-Adaptive} = (0.263, -0.032, 0.080)$  and yield comparable image quality. NUFFT reconstructions show an equivalent behavior and are depicted in Supplementary Figure 3.

## 5 | DISCUSSION

In this work we compared the widely-used AC-Adaptive method without calibration scans [24, 32, 28] for gradient delay estimation in radial imaging with the here introduced Radial INTERsection Gradient delay estimation (RING) method. The advantage of these two methods compared to other trajectory correction approaches is the simple and straightforward implementation while still being robust and accurate. All investigated experiments revealed that RING outperforms the AC-Adaptive method. It particularly possesses three advantages over the AC-Adaptive method:

First and in contrast to RING, the AC-Adaptive method needs (nearly) opposed spokes to determine the shifts via correlation analysis. However, this requirement cannot be fulfilled for half circle acquisitions, where the projection angle is distributed in the range  $\theta \in [0, \pi]$  [34]. We demonstrated this fact in numerical simulations (Fig. 2) for which the



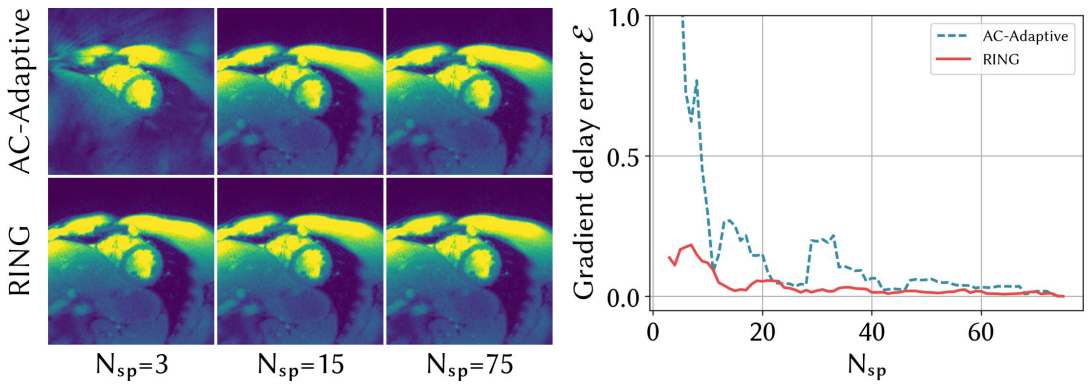


**FIGURE 4** ENLIVE reconstructions using 75 spokes of an in vivo FLASH measurement of the human heart (short-axis view, end-diastole) with gradient delay correction estimated from  $N_{sp}$  number of spokes utilizing the AC-Adaptive method and the RING method. Besides, the gradient delay error  $\mathcal{E}(s_{75}^{est}, s_{N_{sp}}^{est})$  (Eq. (12)) against the number of spokes used for gradient delay estimation is depicted.

AC-Adaptive method provides inaccurate estimates for the gradient delays, whereas RING yields accurate results. Second, the need for opposed spokes in the AC-Adaptive method also prohibits the use of few spokes for gradient delay estimation without calibration scans, if at the same time a uniform k-space coverage shall be guaranteed. We found this notion in all experiments Fig. 2, 3, 4 which show pronounced streaking artifacts and gradient delay errors for few spokes using the AC-Adaptive method, while RING provides high quality results for any number of spokes.

Third, the AC-Adaptive method assumes that gradient delays solely translate into trajectory shifts in readout direction. This, however, is only the case for isotropic delays as shown in Fig. 1. In all other cases, the trajectory additionally experiences an orthogonal shift, which in particular means that even perfectly opposed spokes do not cover the same k-space samples. This also explains why in Fig. 2a) the gradient delay error for the AC-Adaptive method only converges to zero in the isotropic case, but not in the oblique and axial case.

Recently, we have developed an extension to the AC-Adaptive method which allows gradient delay estimation from few spokes by exploiting the conjugate symmetry in k-space instead of finding opposed spokes [32], which, however, suffers from the same model inconsistency concerning orthogonal shifts.

RING requires two parameters:  $N_{pad}$ , which determines the amount of k-space sub-sampling to increase accuracy and  $\beta$  which defines the region in which the samples of the crossing spokes are compared to find the intersection point. In preliminary investigations (not shown) we found that the accuracy of the estimates does not significantly improve for  $N_{pad} > 100$ , so we suggest and used  $N_{pad} = 100$  in all our experiments. In general, gradient delay induced k-space shifts are  $< 0.5 \lambda / \text{FOV}$ , thus the proposed value for  $\beta = 1.5$  is sufficient to find all intersection points. Note, that values  $\beta < 1$  may result in estimation inaccuracies as spokes that are not quite orthogonal could intersect outside of the so defined region. On the other hand, we recommend to never chose  $\beta \gtrsim 4$ , since samples outside of the central k-space contain less energy and are more affected by noise, which might suggest a false intersection point. In the scope of this work we only considered the intersection of a spoke with its most orthogonal counterpart, which is apparently enough to yield valid results. This restriction, however, can be relaxed and the intersection of a spoke with multiple other spokes can be considered in the fit Eq. (10), which can provide minor improvements for very few considered spokes.

RING proofs potential as a general, lightweight on- and offline gradient delay correction tool for radial imaging. Furthermore, it can be used for AC-Adaptive frame-by-frame gradient delay correction in interactive real-time MRI. Because of its flexibility, it can be directly applied to other k-space acquisition schemes based on radials, such as radial simultaneous

multi-slice [37, 38, 39] or stack-of-stars [40, 5].

## 6 | CONCLUSION

We have presented a simple and straight forward new method dubbed RING to estimate gradient delay errors of radial trajectories from very few spokes. RING uses the gradient delay ellipse model introduced by Peters et al. [6] and Moussavi et al. [27] to fit the gradient delays Eq. (3) using the intersection points of spokes. The method yields highly accurate and robust gradient delay estimates even for  $N_{sp} = 3$  spokes in vivo. For its data driven, auto-calibrating nature, it can simply be inserted as a module in existing online or offline frameworks without the need to adapt the measurement protocols.

## 7 | ACKNOWLEDGEMENTS

Supported by the DZHK (German Centre for Cardiovascular Research). Part of this research was funded by the Physics-to-Medicine Initiative Göttingen (LM der Niedersächsischen Vorab) and DFG (UE 189/1-1).

## A | DERIVATION OF THE GRADIENT DELAY ELLIPSE MODEL

First, we recall the definitions and results of [6]. The gradients of the logical system

$$\mathbf{G}_{\theta}^{\log}(t) := \begin{pmatrix} G_{\text{read}}^{\log}(t) \cos \theta \\ G_{\text{read}}^{\log}(t) \sin \theta \\ G_{\text{slice}}^{\log}(t) \end{pmatrix}, \quad (13)$$

can be transformed into the physical system using the orthogonal transform

$$\mathbf{R} := \begin{pmatrix} R_{11} & R_{12} & R_{13} \\ R_{21} & R_{22} & R_{23} \\ R_{31} & R_{32} & R_{33} \end{pmatrix}, \quad (14)$$

which yields

$$\mathbf{G}^{\text{phy}}(t) = \mathbf{R} \mathbf{G}_{\theta}^{\log}(t). \quad (15)$$

The timing delays  $t_x$ ,  $t_y$  and  $t_z$ , that effect the logical gradients, can be modeled using the delay operator

$$\mathcal{T} \mathbf{G}^{\text{phy}}(t) = \begin{pmatrix} G_x^{\text{phy}}(t - t_x) \\ G_y^{\text{phy}}(t - t_y) \\ G_z^{\text{phy}}(t - t_z) \end{pmatrix}. \quad (16)$$

Hence, the delayed gradients in the logical system can be obtained by

$$\tilde{\mathbf{G}}_{\theta}^{\log}(t) = \mathbf{R}^T \mathcal{T} \mathbf{R} \mathbf{G}_{\theta}^{\log}(t), \quad (17)$$

where  $T$  denotes the transpose operation. With definition

$$\mathbf{T} := \frac{\gamma}{2\pi} \begin{pmatrix} t_x & 0 & 0 \\ 0 & t_y & 0 \\ 0 & 0 & t_z \end{pmatrix}, \quad (18)$$

the actual k-space shift is given by

$$\delta \mathbf{k}_{\theta} = \frac{\gamma}{2\pi} \int_0^{\tau} (\tilde{\mathbf{G}}_{\theta}^{\log}(t) - \mathbf{G}_{\theta}^{\log}(t)) dt \quad (19)$$

$$\stackrel{\text{Eq. (15)}}{=} \frac{\gamma}{2\pi} \mathbf{R}^T \int_0^{\tau} (\mathcal{T} \mathbf{G}^{\text{phy}}(t) - \mathbf{G}^{\text{phy}}(t)) dt \quad (20)$$

$$\stackrel{\text{Eq. 16}}{=} \frac{\gamma}{2\pi} \mathbf{R}^T \int_0^{\tau} \begin{pmatrix} G_x^{\text{phy}}(t - t_x) - G_x^{\text{phy}}(t) \\ G_y^{\text{phy}}(t - t_y) - G_y^{\text{phy}}(t) \\ G_z^{\text{phy}}(t - t_z) - G_z^{\text{phy}}(t) \end{pmatrix} dt \quad (21)$$

$$\stackrel{[6]}{=} \mathbf{R}^T \mathbf{T} (\mathbf{G}^{\text{phy}}(\tau) - \mathbf{G}^{\text{phy}}(0)) \quad (22)$$

$$\stackrel{\text{Eq. (15)}}{=} \mathbf{R}^T \mathbf{T} \mathbf{R} (\mathbf{G}_{\theta}^{\log}(\tau) - \mathbf{G}_{\theta}^{\log}(0)) \quad (23)$$

$$\stackrel{\text{Eq. (13)}}{=} \mathbf{R}^T \mathbf{T} \mathbf{R} \begin{pmatrix} G_{\text{read}}^{\log}(\tau) \cos \theta \\ G_{\text{read}}^{\log}(\tau) \sin \theta \\ -G_{\text{slice}}^{\log}(0) \end{pmatrix}. \quad (24)$$

For Eq. (22), we assumed that the temporal delays are small compared to the flattop time of the gradients. In Eq. (24), we used the fact that at the temporal center of the RF pulse ( $t = 0$ ), only the slice selection gradient is active and at the center of readout ( $t = \tau$ ) only the readout gradients are active. We refer the reader to [6] for more details.

In general, we only have information about the projection direction Eq. (2)  $\hat{\mathbf{n}}_{\theta}^{\log} = (\cos \theta, \sin \theta, 0)^T$  and not about the actual gradient strength of a measurement. Therefore, we separate the projection direction using

$$\underline{\mathbf{G}}^{\log} := \begin{pmatrix} G_{\text{read}}^{\log}(\tau) & 0 & 0 \\ 0 & G_{\text{read}}^{\log}(\tau) & 0 \\ 0 & 0 & -G_{\text{slice}}^{\log}(0) \end{pmatrix}, \quad (25)$$

and obtain

$$\delta \mathbf{k}_{\theta} = \mathbf{R}^T \mathbf{T} \mathbf{R} \underline{\mathbf{G}}^{\log} (\hat{\mathbf{e}}_z^{\log} + \hat{\mathbf{n}}_{\theta}^{\log}), \quad (26)$$

with  $\hat{\mathbf{e}}_z^{\log} = (0, 0, 1)^T$ .

The first term of the right-hand-side of Eq. (26) is independent of the angle and thus does not effect the ellipse fit of RING and corresponds to a constant k-space offset, i.e. a linear phase in image space, and can therefore be neglected.

Then, Eq. (26) written out is given by

$$\delta \mathbf{k}_\theta \approx \mathbf{R}^T \mathbf{T} \mathbf{R} \mathbf{G}^{\log} \hat{\mathbf{n}}_\theta^{\log} \quad (27)$$

$$= \begin{pmatrix} G_{\text{read}}^{\log}(t_x R_{11}^2 + t_y R_{21}^2 + t_z R_{31}^2) & G_{\text{read}}^{\log}(t_x R_{11} R_{12} + t_y R_{21} R_{22} + t_z R_{31} R_{32}) & G_{\text{slice}}^{\log}(t_x R_{11} R_{13} + t_y R_{21} R_{23} + t_z R_{31} R_{33}) \\ G_{\text{read}}^{\log}(t_x R_{12} R_{11} + t_y R_{22} R_{21} + t_z R_{32} R_{31}) & G_{\text{read}}^{\log}(t_x R_{12}^2 + t_y R_{22}^2 + t_z R_{32}^2) & G_{\text{slice}}^{\log}(t_x R_{12} R_{13} + t_y R_{22} R_{23} + t_z R_{32} R_{33}) \\ G_{\text{read}}^{\log}(t_x R_{13} R_{11} + t_y R_{23} R_{21} + t_z R_{33} R_{31}) & G_{\text{read}}^{\log}(t_x R_{12} R_{13} + t_y R_{22} R_{23} + t_z R_{32} R_{33}) & G_{\text{slice}}^{\log}(t_x R_{13}^2 + t_y R_{23}^2 + t_z R_{33}^2) \end{pmatrix} \begin{pmatrix} \cos \theta \\ \sin \theta \\ 0 \end{pmatrix}. \quad (28)$$

Here, we are only interested in the in-plane gradient delays, for which it suffices to consider the top left  $2 \times 2$  submatrix. By substitution we yield Eq. (1)

$$\delta \mathbf{k}_\theta \approx \begin{pmatrix} G_{\text{read}}^{\log}(t_x R_{11}^2 + t_y R_{21}^2 + t_z R_{31}^2) & G_{\text{read}}^{\log}(t_x R_{11} R_{12} + t_y R_{21} R_{22} + t_z R_{31} R_{32}) \\ G_{\text{read}}^{\log}(t_x R_{12} R_{11} + t_y R_{22} R_{21} + t_z R_{32} R_{31}) & G_{\text{read}}^{\log}(t_x R_{12}^2 + t_y R_{22}^2 + t_z R_{32}^2) \end{pmatrix} \hat{\mathbf{n}}_\theta^{\log} \quad (29)$$

$$:= \begin{pmatrix} S_x & S_{xy} \\ S_{xy} & S_y \end{pmatrix} \hat{\mathbf{n}}_\theta^{\log}. \quad (30)$$

## REFERENCES

- [1] Song HK, Dougherty L. k-Space weighted image contrast (KWIC) for contrast manipulation in projection reconstruction MRI. *Magn. Reson. Med.* 2000; 44:825–832.
- [2] Mistretta CA, Wieben O, Velikina J, Block W, Perry J, Wu, Y, Johnson K, Wu Y. Highly constrained backprojection for time-resolved MRI. *Magn. Reson. Med.* 2006; 55:30–40.
- [3] Uecker M, Zhang S, Frahm J. Nonlinear inverse reconstruction for real-time MRI of the human heart using undersampled radial FLASH. *Magn. Reson. Med.* 2010; 63:1456–1462.
- [4] Wright KL, Hamilton JI, Griswold MA, Gulani V, Seiberlich N. Non-Cartesian parallel imaging reconstruction. *J. Magn. Reson. Imaging* 2014; 40:1022–1040.
- [5] Block KT, Chandarana H, Milla S, Bruno M, Mulholland T, Fatterpekar G, Hagiwara M, Grimm R, Geppert C, Kiefer B. Towards routine clinical use of radial stack-of-stars 3d gradient-echo sequences for reducing motion sensitivity. *J. Korean Soc. Magn. Reson. Med.* 2014; 18:87–106.
- [6] Peters DC, Derbyshire JA, McVeigh ER. Centering the projection reconstruction trajectory: Reducing gradient delay errors. *Magn. Reson. Med.* 2003; 50:1–6.
- [7] Barmet C, Zanche ND, Pruessmann KP. Spatiotemporal magnetic field monitoring for MR. *Magn. Reson. Med.* 2008; 60:187–197.
- [8] Dietrich BE, Brunner DO, Wilm BJ, Barmet C, Gross S, Kasper L, Haeberlin M, Schmid T, Vannesjo SJ, Pruessmann KP. A field camera for MR sequence monitoring and system analysis. *Magn. Reson. Med.* 2016; 75:1831–1840.
- [9] Vannesjo SJ, Haeberlin M, Kasper L, Pavan M, Wilm BJ, Barmet C, Pruessmann KP. Gradient system characterization by impulse response measurements with a dynamic field camera. *Magn. Reson. Med.* 2013; 69:583–593.
- [10] Liu H, Matson GB. Accurate measurement of magnetic resonance imaging gradient characteristics. *Materials* 2014; 7:1–15.
- [11] Jang H, McMillan AB. A rapid and robust gradient measurement technique using dynamic single-point imaging. *Magn. Reson. Med.* 2016; DOI: 10.1002/mrm.26481.
- [12] Stich M, Wech T, Slawig A, Ringler R, Dewdney A, Greiser A, Ruyters G, Bley TA, Köstler H. Gradient waveform pre-emphasis based on the gradient system transfer function. *Magn. Reson. Med.* 2018; DOI: 10.1002/mrm.27147.

- [13] Deshmane A, Blaimer M, Breuer F, Jakob P, Duerk J, Seiberlich N, Griswold M. Self-calibrated trajectory estimation and signal correction method for robust radial imaging using GRAPPA operator gridding. *Magn. Reson. Med.* 2016; 75:883–896.
- [14] Wech T, TranGia J, Bley TA, Köstler H. Using self-consistency for an iterative trajectory adjustment (SCITA). *Magn. Reson. Med.* 2015; 73:1151–1157.
- [15] Seiberlich N, Breuer FA, Blaimer M, Barkauskas K, Jakob PM, Griswold MA. Non-Cartesian data reconstruction using GRAPPA operator gridding (GROG). *Magn. Reson. Med.* 2007; 58:1257–1265.
- [16] Kerr AB, M. PJ, S. HB, C. LK, J. HC, H. MC, Albert M, G. ND. Real-time interactive MRI on a conventional scanner. *Magn. Reson. Med.* 1997; 38:355–367.
- [17] Guttman MA, Peter K, J. DA, J. LR, R. ME. Real-time accelerated interactive MRI with adaptive TSENSE and UNFOLD. *Magn. Reson. Med.* 2003; 50:315–321.
- [18] Yang PC, Kerr AB, Liu AC, Liang DH, Hardy C, Meyer CH, Macovski A, Pauly JM, Hu BS. New real-time interactive cardiac magnetic resonance imaging system complements echocardiography. *J Am Coll Cardiol* 1998; 32:2049 – 2056.
- [19] Unterberg-Buchwald C, Ritter CO, Reupke V, Wilke RN, Stadelmann C, Steinmetz M, Schuster A, Hasenfuß G, Lotz J, Uecker M. Targeted endomyocardial biopsy guided by real-time cardiovascular magnetic resonance. *J. Cardio. Magn. Reson.* 2017; 19:45.
- [20] Jiang W, Larson PE, Lustig M. Simultaneous auto-calibration and gradient delays estimation (SAGE) in non-Cartesian parallel MRI using low-rank constraints. *Magn. Reson. Med.* 2018; DOI: 10.1002/mrm.27168.
- [21] Shin PJ, Larson PEZ, Ohliger MA, Elad M, Pauly JM, Vigneron DB, Lustig M. Calibrationless parallel imaging reconstruction based on structured low-rank matrix completion. *Magn. Reson. Med.* 2014; 72:959–970.
- [22] Mani M, Magnotta V, Jacob M. A general algorithm for compensation of trajectory errors: Application to radial imaging. *Magn. Reson. Med.* 2018; DOI: 10.1002/mrm.27148.
- [23] Ianni JD, Grissom WA. Trajectory Auto-Corrected image reconstruction. *Magn. Reson. Med.* 2016; 76:757–768.
- [24] Block KT, Uecker M. Simple Method for Adaptive Gradient-Delay Compensation in Radial MRI. In: *Proc. Intl. Soc. Mag. Reson. Med.* 19, Montreal, 2011. p. 2816.
- [25] Feng L, Grimm R, Block KT, Chandarana H, Kim S, Xu J, Axel L, Sodickson DK, Otazo R. Golden-angle radial sparse parallel MRI: Combination of compressed sensing, parallel imaging, and golden-angle radial sampling for fast and flexible dynamic volumetric MRI. *Magn. Reson. Med.* 2014; 72:707–717.
- [26] Wundrak S, Paul J, Ulrici J, Hell E, Rasche V. A small surrogate for the golden angle in time-resolved radial MRI based on generalized fibonacci sequences. *IEEE Trans Med Imag* 2015; 34:1262–1269.
- [27] Moussavi A, Untenberger M, Uecker M, Frahm J. Correction of gradient-induced phase errors in radial MRI. *Magn. Reson. Med.* 2013; 71:308–312.
- [28] Untenberger M, Tan Z, Voit D, Joseph AA, Roeloffs V, Merboldt KD, Schätz S, Frahm J. Advances in real-time phase-contrast flow MRI using asymmetric radial gradient echoes. *Magn. Reson. Med.* 2016; 75:1901–1908.
- [29] Wang X, Roeloffs V, Klosowski J, Tan Z, Voit D, Uecker M, Frahm J. Model-based T1 mapping with sparsity constraints using single-shot inversion-recovery radial FLASH. *Magn. Reson. Med.* 2018; 79:730–740.
- [30] Schaetz S, Voit D, Frahm J, Uecker M. Accelerated Computing in Magnetic Resonance Imaging: Real-Time Imaging Using Nonlinear Inverse Reconstruction. *Comput Math Method M* 2017; DOI: 10.1155/2017/3527269.

- [31] Volkert R, Xiaoqing W, J. ST, Markus U, Dirk V, Jens F. Model-based reconstruction for T1 mapping using single-shot inversion-recovery radial FLASH. *Int. J. Imag. Syst. Tech.* 2016; 26:254–263.
- [32] Rosenzweig S, Holme HCM, Wilke RN, Uecker M. Extending the Simple Method for Adaptive Gradient-Delay Compensation in Radial MRI. In: *Proc. Intl. Soc. Mag. Reson. Med.* 26, Paris, 2018.
- [33] Uecker M, Ong F, Tamir JI, Bahri D, Virtue P, Cheng JY, Zhang T, Lustig M. Berkeley advanced reconstruction toolbox. In: *Proc. Intl. Soc. Mag. Reson. Med.* 23, Toronto, 2015. p. 2486.
- [34] Haji-Valizadeh H, Rahsepar AA, Collins JD, Bassett E, Isakova T, Block T, Adluru G, DiBella EVR, Lee DC, Carr JC, Kim D, with Binders TCOM, Group NCS. Validation of highly accelerated real-time cardiac cine MRI with radial k-space sampling and compressed sensing in patients at 1.5T and 3T. *Magn. Reson. Med.* 2018; 79:2745–2751.
- [35] Uecker M, Hohage T, Block KT, Frahm J. Image reconstruction by regularized nonlinear inversion—joint estimation of coil sensitivities and image content. *Magn. Reson. Med.* 2008; 60:674–682.
- [36] Holme HCM, Rosenzweig S, Ong F, Wilke RN, Lustig M, Uecker M. ENLIVE: An Efficient Nonlinear Method for Calibrationless and Robust Parallel Imaging. *ArXiv* 2017; arXiv:1706.09780.
- [37] Wang H, Adluru G, Chen L, Kholmovski EG, Bangerter NK, DiBella EVR. Radial simultaneous multi-slice CAIPI for ungated myocardial perfusion. *Magn. Reson. Imaging* 2016; 34:1329 – 1336.
- [38] Rosenzweig S, Holme HCM, Wilke RN, Uecker M. Simultaneous Multi-Slice Real-Time Imaging with Radial Multi-Band FLASH and Nonlinear Inverse Reconstruction. In: *Proc. Intl. Soc. Mag. Reson. Med.* 25, Honolulu, 2017. p. 0518.
- [39] Rosenzweig S, Holme HCM, Wilke RN, Voit D, Frahm J, Uecker M. Simultaneous multi-slice MRI using cartesian and radial FLASH and regularized nonlinear inversion: SMS-NLINV. *Magn. Reson. Med.* 2018; 79:2057–2066.
- [40] Zhou Z, Han F, Yan L, Wang DJ, Hu P. Golden-ratio rotated stack-of-stars acquisition for improved volumetric MRI. *Magn. Reson. Med.* 2017; DOI: 10.1002/mrm.26625.

## 1 | ACCURACY OF THE INTERSECTION POINT DETERMINATION

We perform phantom simulations with different numerical phantoms, signal to noise ratios and numbers of coils to analyze the accuracy of the intersection point determination using a pixel-wise comparison of the spokes' samples.

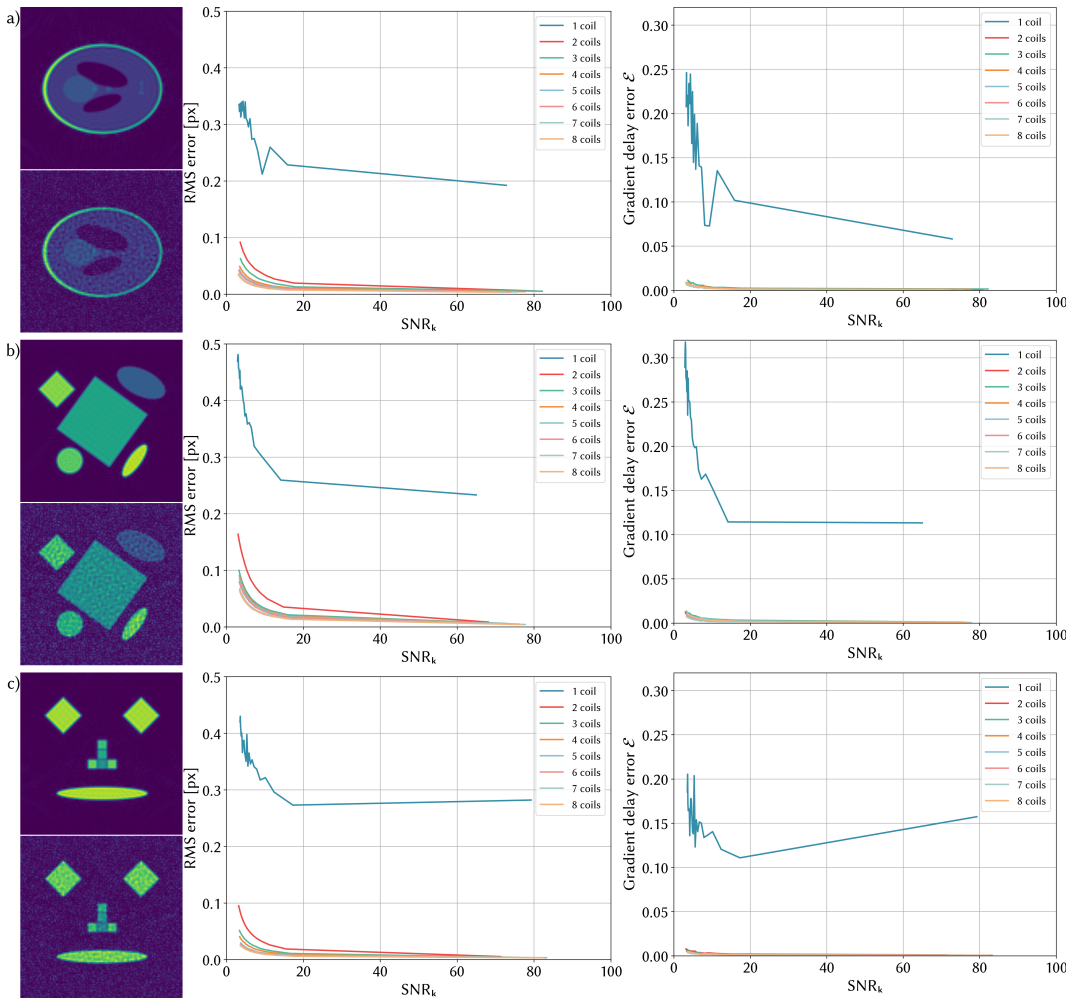
We utilize a Shepp-Logan phantom and two other geometric phantoms. The left side of Sup. Fig. 1 shows NUFFT reconstructions of the phantoms for different signal to noise ratios. We simulate the corresponding delayed radial k-space data ( $s := (0.3, -0.1, 0.2)$ , full circle golden angle trajectory, 160 read-out samples, 159 spokes) for  $c = 1, \dots, 8$  coils and add Gaussian white noise. As a measure for the noise we divide the energy of the noise-free k-space by the energy of the added noise:  $\text{SNR}_k = E_s/E_n$ . We compare all actual intersection points with the estimated intersection point using Eq. (4,5) and  $s$ . For the estimation, the values for  $a_{\theta_j}$  are determined by pixelwise comparison of the spokes' samples as described in the manuscript. The analytical expression used to determine the actual intersection point can be derived using Eq. (5):

$$a_{\theta_j} = \begin{pmatrix} \hat{n}_{\theta_{j,2}} \\ \hat{n}_{\theta_{j,2}}\hat{n}_{\theta_{j,1}} - \hat{n}_{\theta_{j,1}} \end{pmatrix} \begin{pmatrix} S_x \xi_1 + S_{xy} \xi_2 - \frac{\hat{n}_{\theta_{j,1}}}{\hat{n}_{\theta_{j,2}}} (S_{xy} \xi_1 + S_y \xi_2) \end{pmatrix}.$$

The central column of Sup. Fig. 1 shows the root-mean-square (RMS) error between all measured and actual intersection points for different noise levels and numbers of coils.

Furthermore, we estimate the gradient delays  $s_{\text{SNR}_k, c}^{\text{est}}$  for the same numbers of coils  $c$  and signal to noise ratios. The gradient delay error  $\mathcal{E}(s, s_{\text{SNR}_k, c}^{\text{est}})$  (Eq. (12)) is depicted in Sup. Fig. 1, right column.

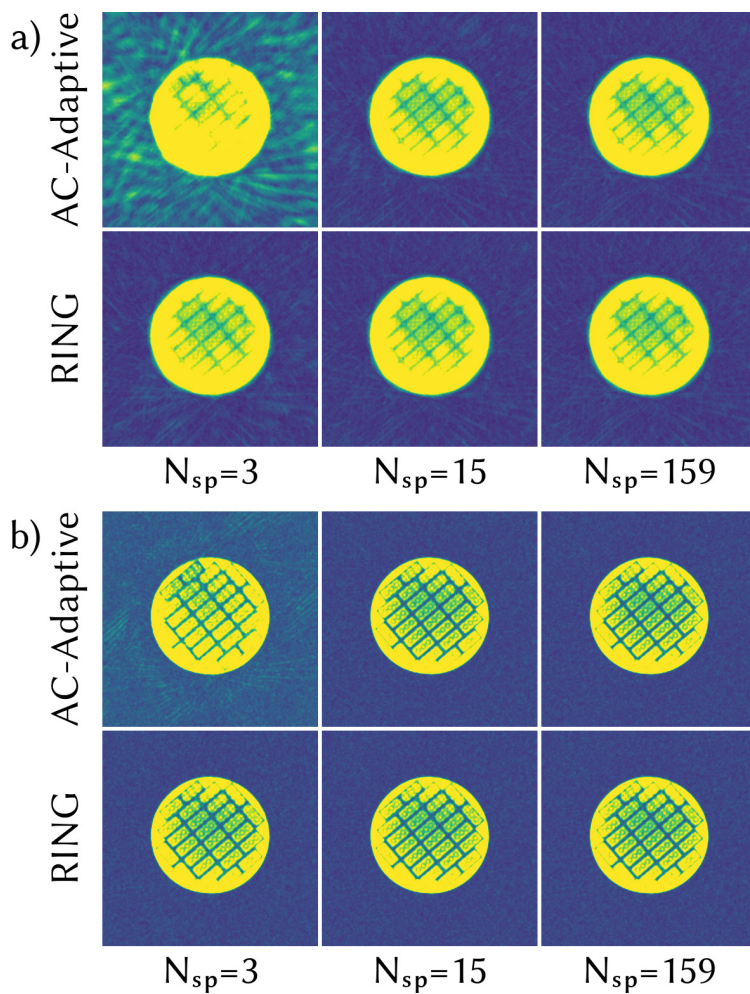
Both the gradient delay error and the RMS error of the intersection points improve with the number of utilized coils. This behavior is sensible as samples from all channels can be used to determine the intersection points and thus more robust results can be obtained. While a single coil yields bad results for any noise level, the use of multiple coils, which today is clinical standard, yield accurate results even for low  $\text{SNR}_k$  values. The accuracy is comparable for all investigated phantoms.



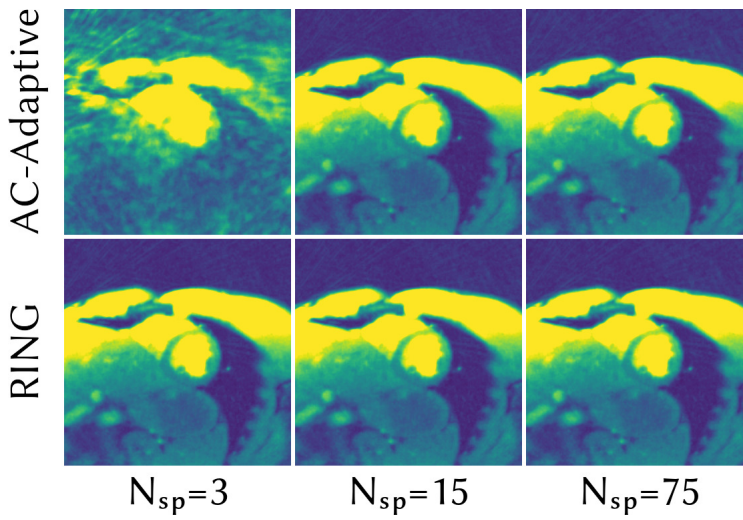
**SUP. FIGURE 1** Intersection point accuracy analysis for three different numerical phantoms a), b), c). Left: NUFFT reconstructions without noise and with  $\text{SNR}_k \approx 7$ . Center: Root-mean-square error of the measured intersection point against the  $\text{SNR}_k$  for different numbers of coils. Right: Gradient delay estimation error against the  $\text{SNR}_k$  for different numbers of coils.



## 2 | NUFFT RECONSTRUCTIONS



**SUP. FIGURE 2** NUFFT reconstructions of a brick phantom FLASH measurement with gradient delay correction estimated from  $N_{sp}$  number of spokes utilizing the AC-Adaptive method and the RING method. a) 39 spokes used for reconstruction. b) 159 spokes used for reconstruction.



**SUP. FIGURE 3** NUFFT reconstructions using 75 spokes of an in vivo FLASH measurement of the human heart (short-axis view, end-diastole) with gradient delay correction estimated from  $N_{sp}$  number of spokes utilizing the AC-Adaptive method and the RING method.